SUPPLEMENTARY FIGURES

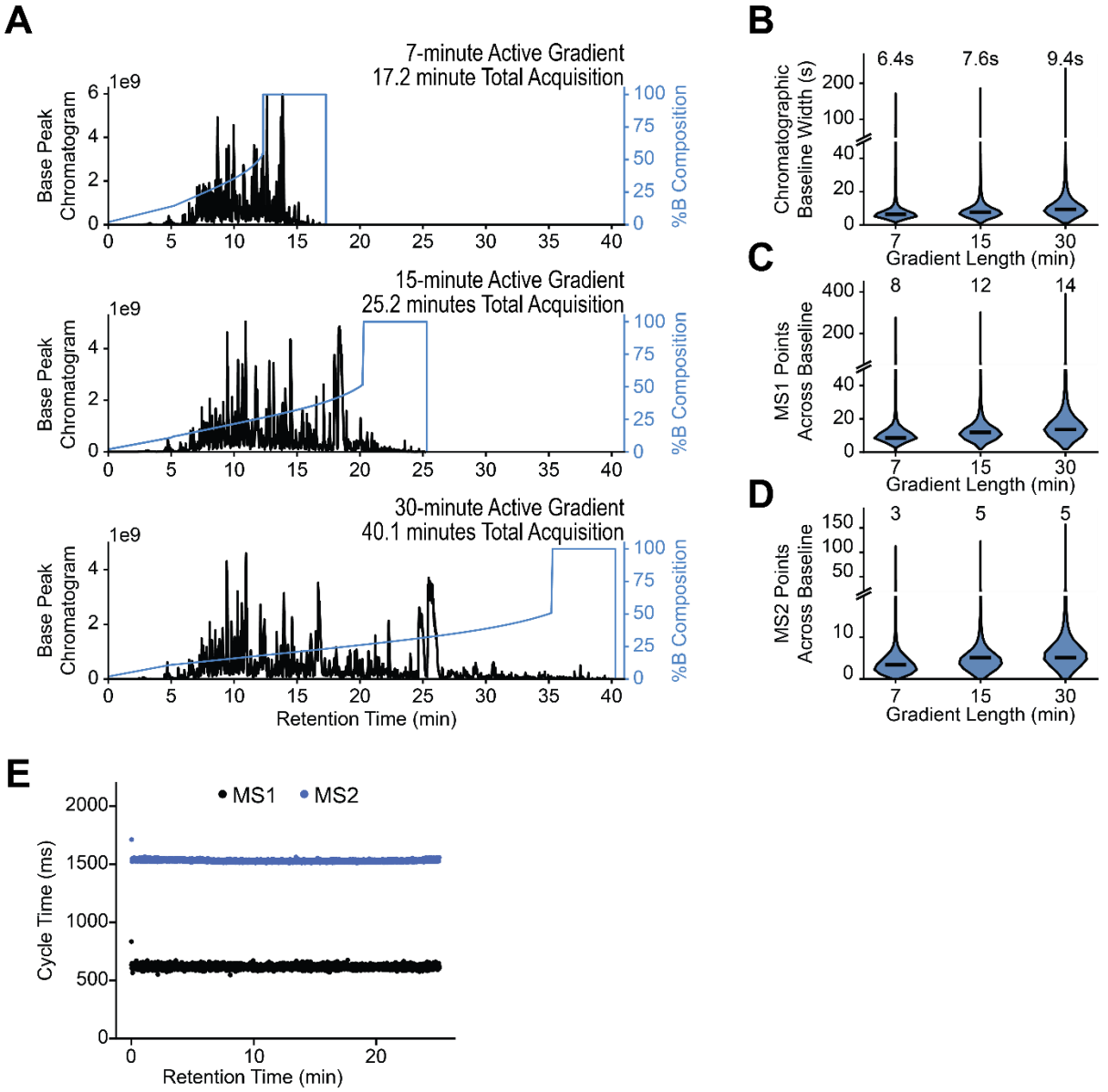

Supplementary Figure 1. Chromatographic Properties of HEK293T Phosphoproteomics Datasets (A) Representative chromatograms for different gradient lengths. The base peak chromatograms for the three different active gradient lengths are shown with the gradient composition curve plotted. The distribution of (B) chromatographic baseline widths, (C) MS1 points across the baseline peak, and (D) MS2 points across the baseline peaks are shown with the median value indicated in the violin plot and printed above for three different active gradient lengths. The values were estimated by multiplying chromatographic FWHM, MS1 points across FWHM, and MS2 points across FWHM reported by Spectronaut 17 by 1.7 (based on the 4σ baseline width of a Gaussian distribution where 4σ ≈1.7 * FWHM). (E) The cycle times for the MS1 and MS2 scan sequences are shown as a function of RT. Source Data are provided as a Source Data file.

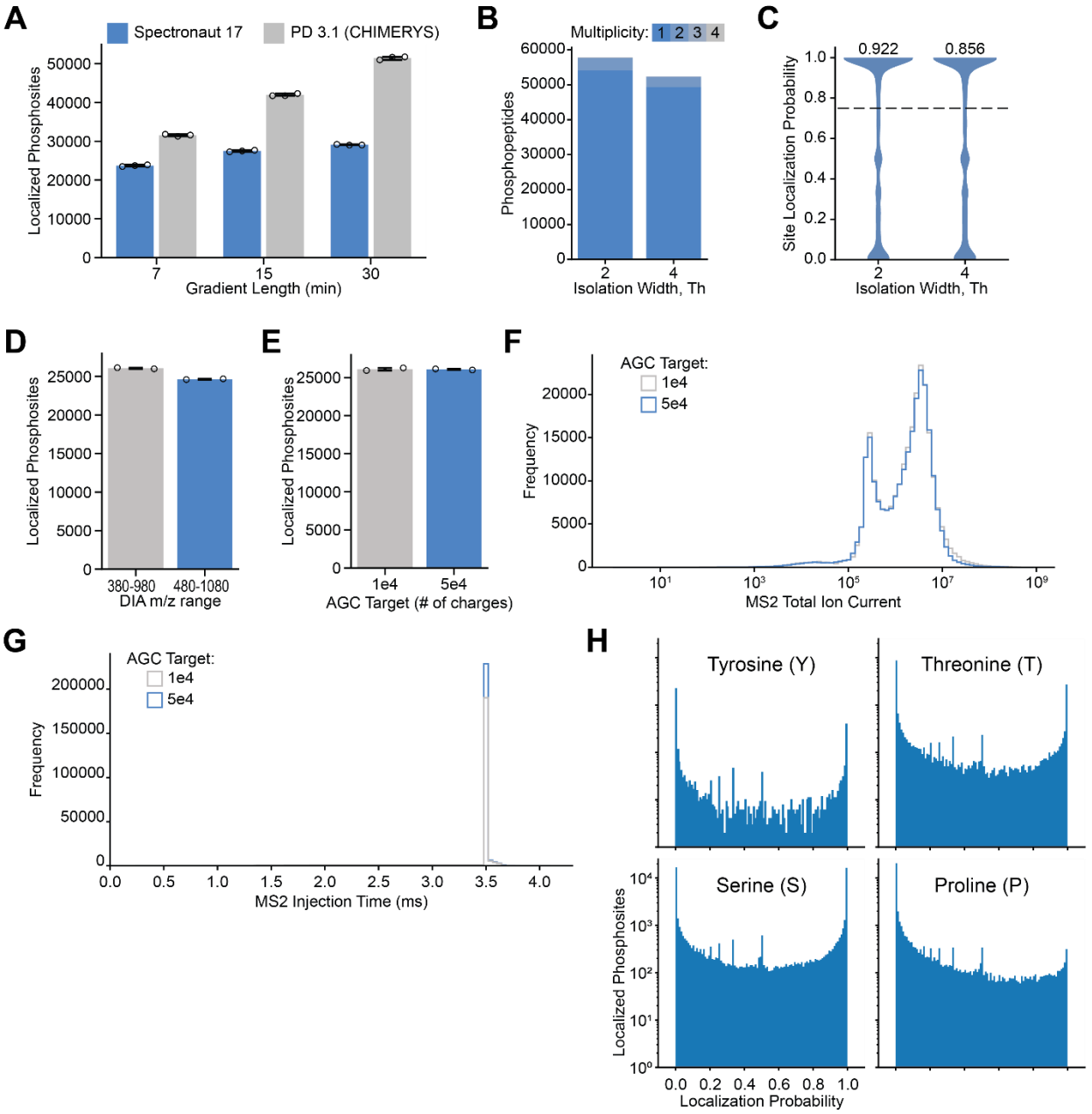

Supplementary Figure 2. Evaluation of Phosphoproteomic Method and Processing Parameters. (A) The average number of localized phosphosites across triplicate injections for three different gradient lengths is shown for searches in Spectronaut (blue) and CHIMERYS in Proteome Discoverer 3.1 (gray). The error bars represent the maximum and minimum value across the triplicates. (B) The average number of phosphopeptides and multiplicity distributions are shown for the data in **Figure 2B**. (C) The site localization probability distributions are shown for the data in **Figure 2B** with the median value indicated above. (D) The average number of phosphosites detected across two replicate injections in EGF-stimulated HeLa cells are shown for two different DIA *m/z* ranges. Error bars indicated the maximum and minimum number of phosphosites. (E) The average number of phosphosites detected across two replicate injections in EGF-stimulated HeLa cells are shown for two different AGC target values. Error bars indicated

the maximum and minimum number of phosphosites. (F) The MS2 total ion current distributions are indicated for the two AGC targets in **Supplementary Figure 2E**. (G) The distributions of MS2 injection times are indicated for the two AGC targets in **Supplementary Figure 2E**. (H) Histograms of localization probabilities for S, T, Y, and P residues are shown as an alternative visualization for the phosphoproline decoy search results in **Figure 2H**. Source Data are provided as a Source Data file.

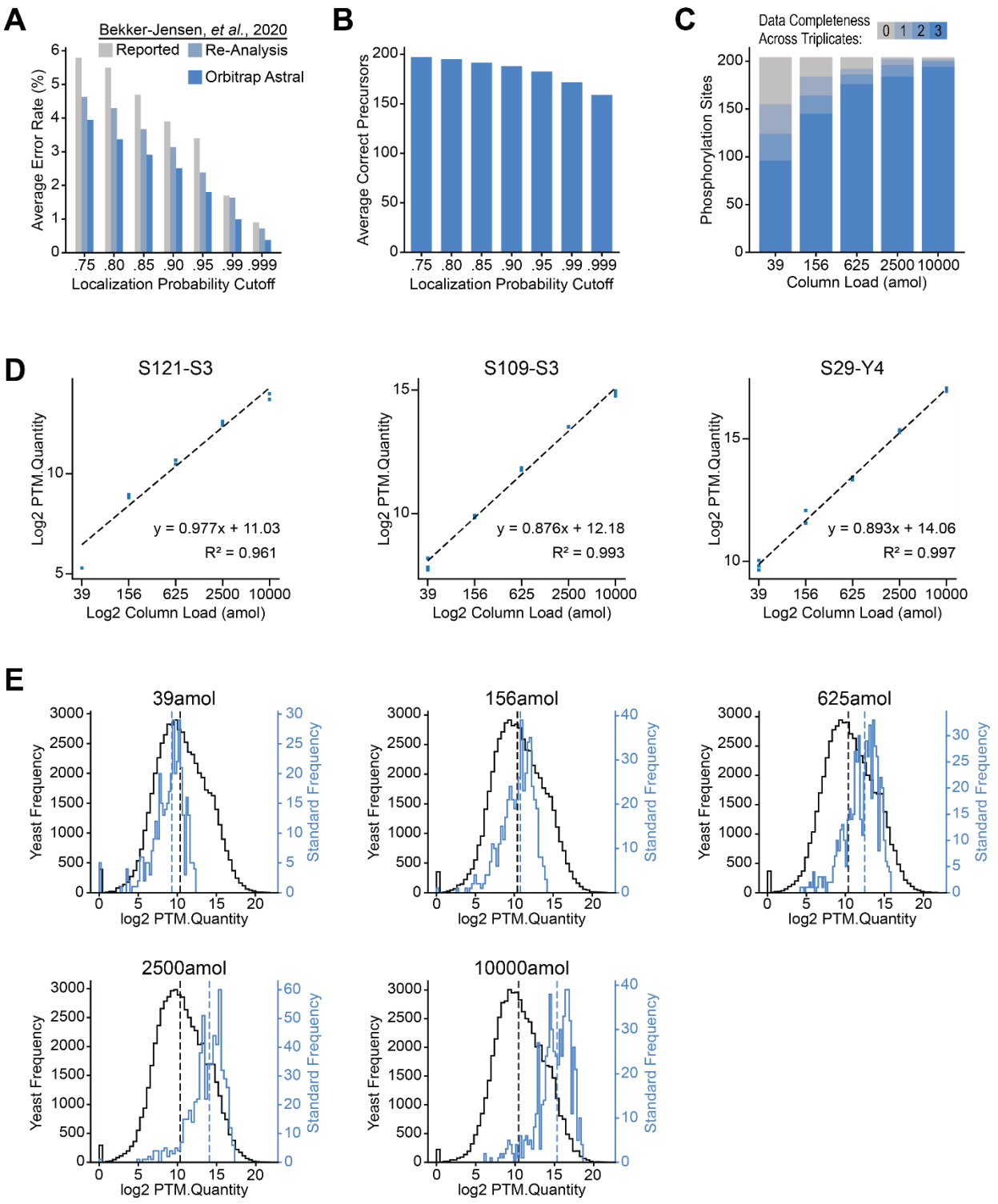

Supplementary Figure 3. **Validation of Site Localization and Quantification using Synthetic Phosphopeptide Standards**. (A) The localization error rates shown in **Figure 2I** are compared to the values previously reported by Bekker-Jensen *et al*[1] alongside the error rates calculated following re-analysis of the data from Bekker-Jensen *et al* with the same protein database and Spectronaut workflow used in this study. (B) The average number of correctly identified precursors as a function of localization probability cutoff are

shown for the dataset in **Figure 2I**. (C) The detection completeness of synthetic phosphosites across triplicate injections is shown as a function of the column load for the data in **Figure 2J**. (D) Calibrations curves for three randomly selected synthetic phosphosites are shown from the synthetic phosphopeptides dilution series dataset. 'S121-S3' indicates the phosphorylation serine at position 3 for phosphopeptide standard 121. (E) The distribution of phosphosite intensities (Spectronaut's PTM.Quantity value) for the synthetic phosphopeptide standards and yeast phosphopeptides are shown in blue and black, respectively, for each of the dilution series points. The median intensity for the phosphopeptide standards and yeast phosphopeptides is indicated on each plot with a blue and black dotted line, respectively. Source Data are provided as a Source Data file.

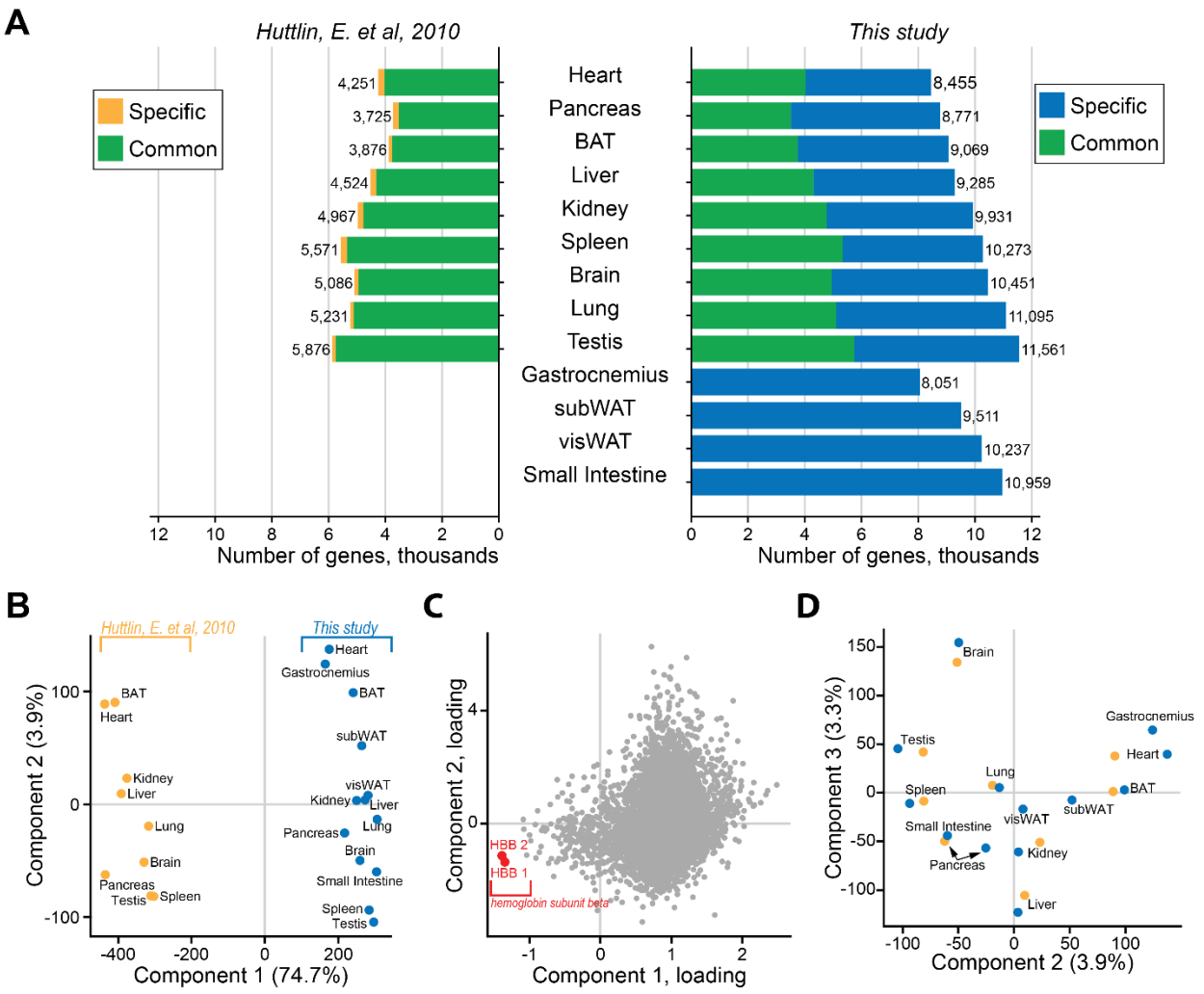

Supplementary Figure 4. Proteomic Profiling of Mouse Tissues. (A) Results from Mouse Tissue Proteomic Analysis. The numbers of protein groups are indicated for each tissue, with common protein groups highlighted in green, those unique to Huttlin *et al.* in yellow, and those unique to this study in blue. The Huttlin *et al.* results were generated by analyzing raw data in MaxQuant, employing the same protein database utilized in this study. (B) Principal Component Analysis (PCA) based on protein expression of common proteins between two studies. (C) PCA loading plot of first two components from (B) with highlights of HBB1 and HBB2 proteins. (D) The same PCA as (B) but Component 2 and Component 3 visualized.

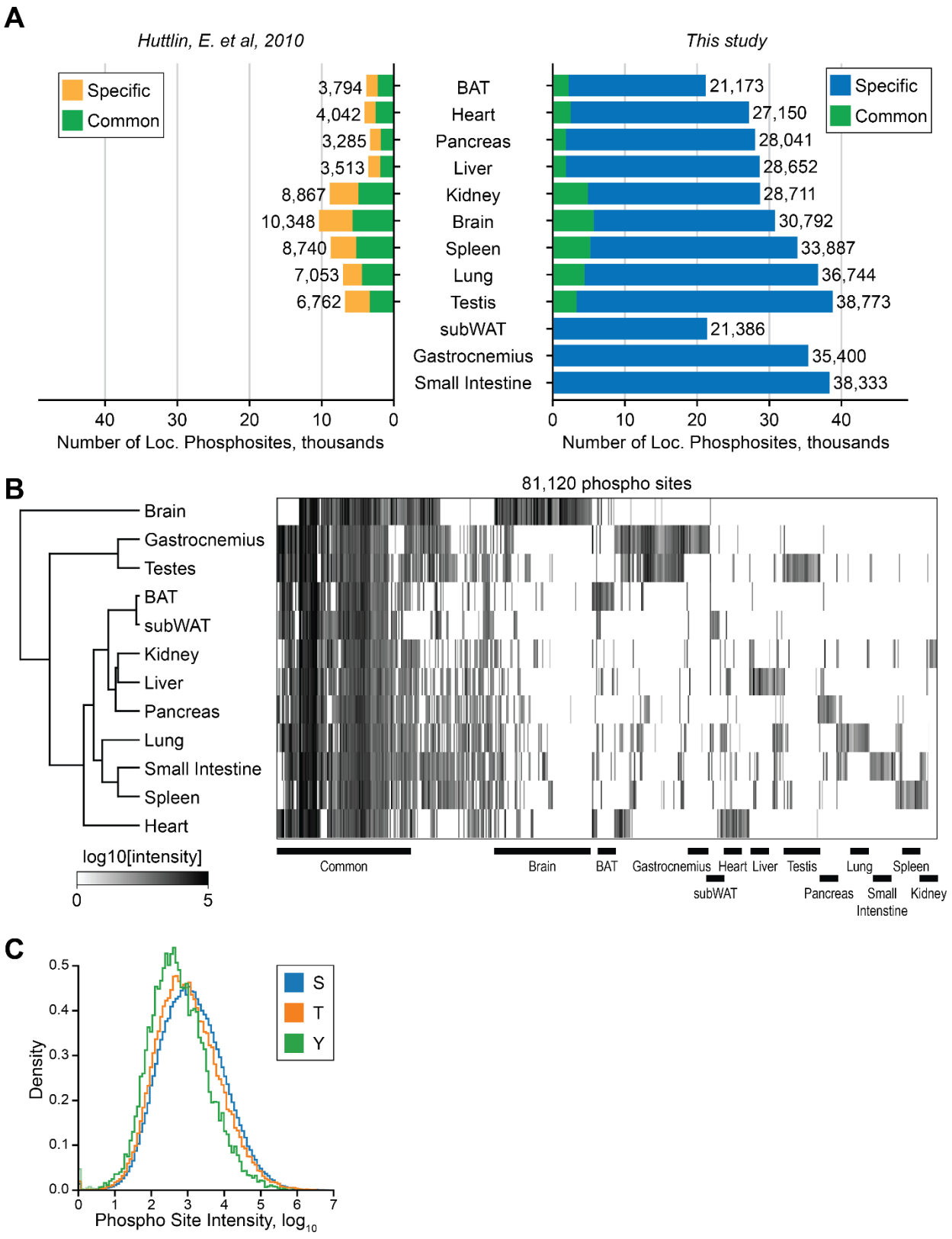

Supplementary Figure 5. Mouse Phosphorylation Atlas Comparison to Huttlin et al. (A) Overlap of phosphorylation sites detected in this study and by Huttlin *et al.*[2] (B) Heatmap showing the relative intensities of phosphosites detected across tissues. Note

that there are many phosphorylation sites with similar intensities across all tissues, but each tissue tends to have clusters of phosphosites that are uniquely high intensity (C) Normalized distribution of phosphorylation site intensities for S, T, and Y localizations.

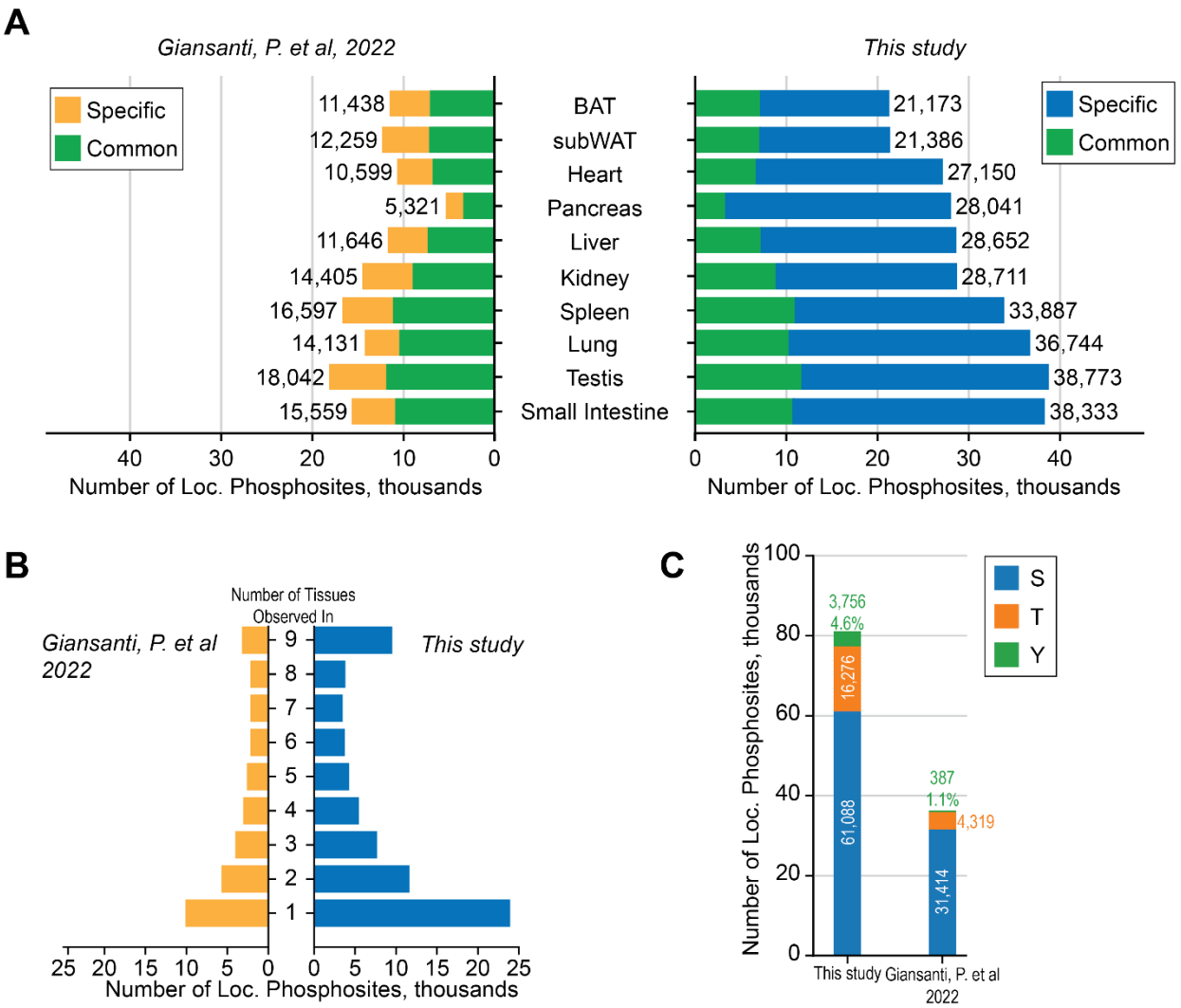

Supplementary Figure 6. Mouse Phosphorylation Atlas Comparison to Giansanti *et al*. (A) Overlap of phosphorylation sites detected in this study and by Giansanti *et al*.[3] (B) Tissue Specificity of Detected Phosphorylation sites, excluding the pancreas, brain, and gastrocnemius tissues from comparison. The y-axis indicates the number of tissues in which a phosphosite was detected. (C) The total number of S, T, Y phosphorylation sites are shown for this study and Giansanti *et al*.[3] The percentage of the total sites occurring on phosphotyrosine residues is indicated for both studies.

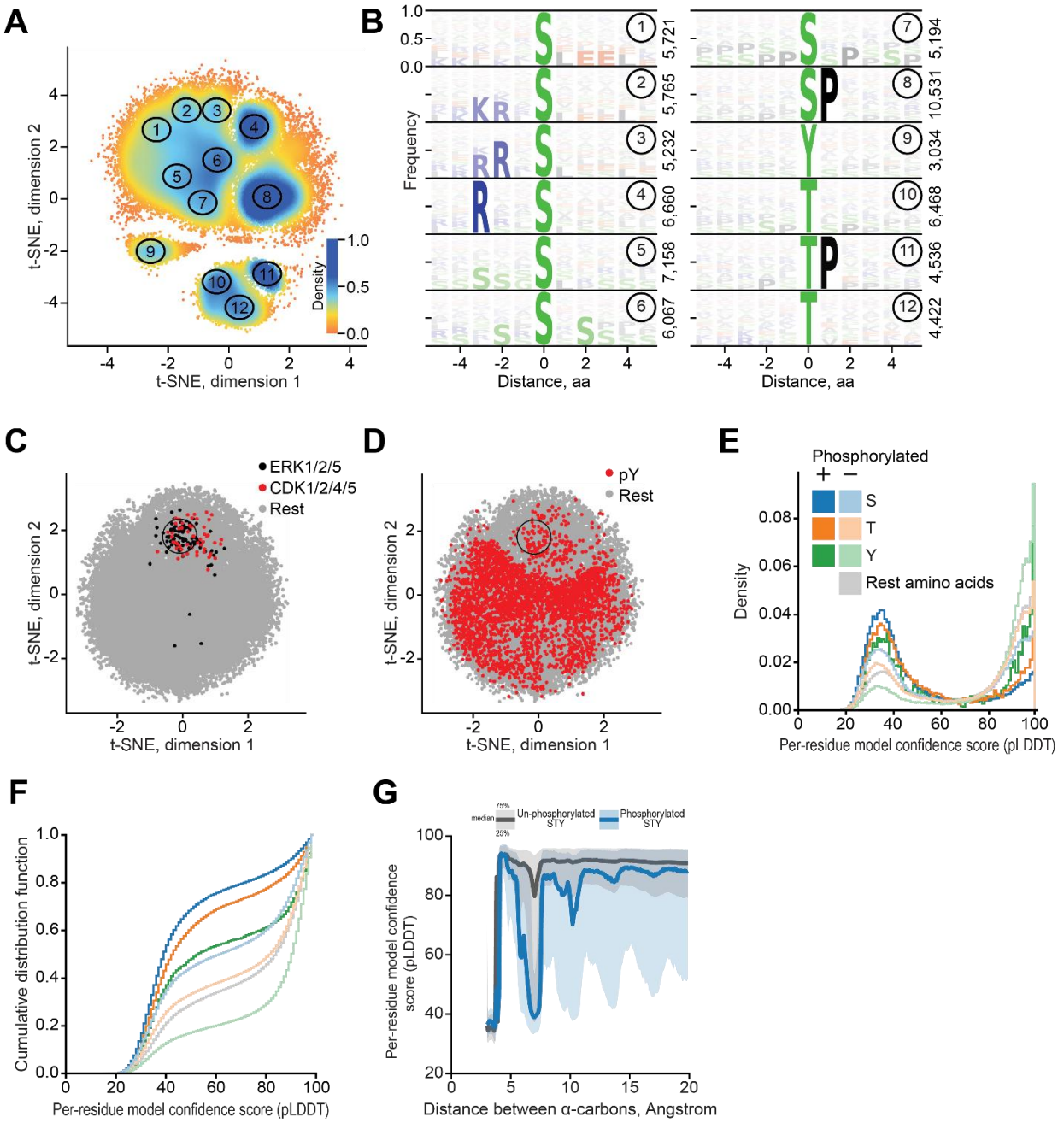

Supplementary Figure 7. Sequence and Structural Context of Phosphosites. (A) Two-dimensional representation of all phosphosites and their 5-amino acid flanking sequences, including the central amino acid in the comparison. Each cluster has been manually selected to highlight the densest regions. (B) Sequence logo plot for all clusters depicted in (A). (C) Similar to Figure 5A with highlights of ERK and CDK kinases based on the PhosphoSitePlus database. (D) Similar to Figure 5A with highlights of all phosphorylated tyrosine sites. (E) Distribution of structural confidence scores for phosphorylated (+) and unphosphorylated STY sites. (F) Similar to (E) but presented as a cumulative distribution plot. (G) Confidence score distribution based on the distance

between alpha-carbons surrounding phosphorylation site and phosphorylation state – phosphorylated and un-phosphorylated S/T/Y.

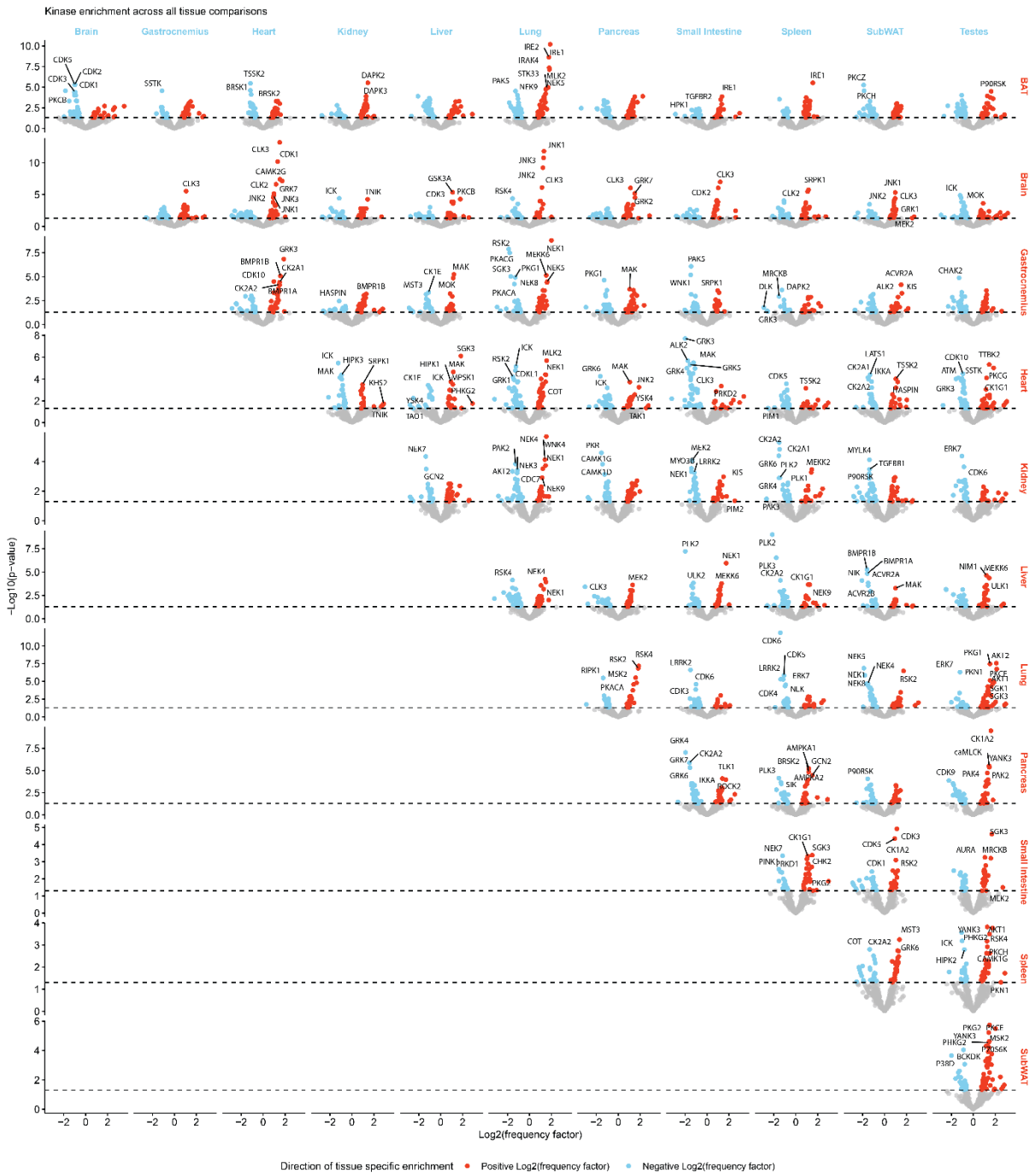

Supplementary Figure 8. Kinase Enrichment Across Tissues. For each possible tissue-tissue pair, the top tissue-specific phosphorylation sites were selected to perform a kinase motif enrichment analysis. The frequency of how often a kinase was predicted to act on a site in a tissue was plotted on the x-axis. The p-value is shown on the y-axis. The red dots indicate significant kinases in the tissues that are labelled in red on the right side of the plot. The blue dots correspond to the tissues plotted across the top of the graph. The p-values were calculated using a chi-squared test on the data set after applying Haldane's correction to compare the frequency factors for each kinase in each

tissue. The frequency factor was calculated as the proportion of how often a kinase was predicted within the top phosphorylation sites versus the total of top phosphorylation sites, divided by the same ratio for the unchanged sites, i.e., not ranked among the top/bottom 200 (with regards to z-score). Source data is provided in **Supplementary Data 5**.

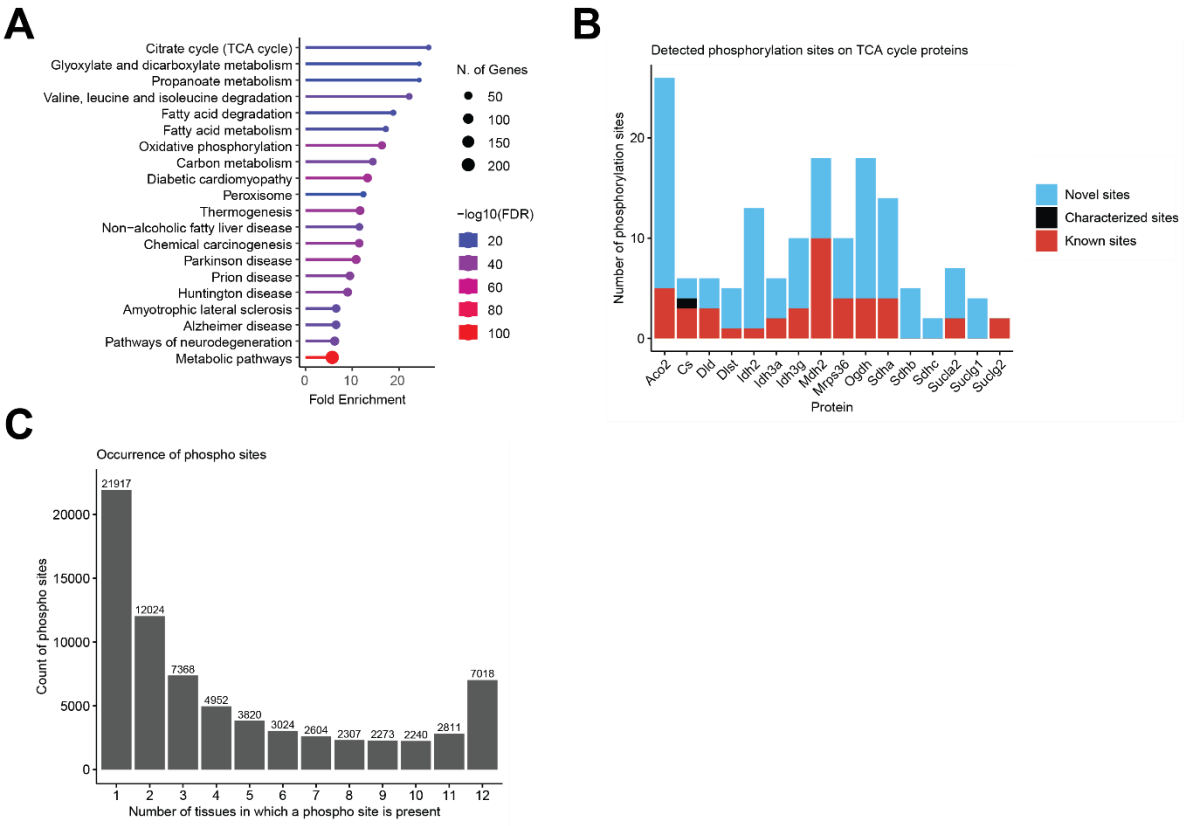

Supplementary Figure 9. TCA cycle phosphorylation events and occurrence of phosphorylation sites across tissues. (A) GSEA using the KEGG pathway database, FDR 0.05, minimal pathway size 2, through the ShinyGO app.[4] Input: Proteins whose phosphorylation sites showed an absolute z-score above 2. (B) Number of phosphorylation sites detected on tricarboxylic cycle proteins (subset based on MitoCarta 3.0 pathways). Sites that occur in multiple tissues are summed. Characterized sites according to PhosphoSitePlus are also known sites and are only counted in the characterized sites category. (C) Bar plot indicating the number of phosphorylation sites that occur in a specific number of tissues. Source Data are provided as a Source Data file.

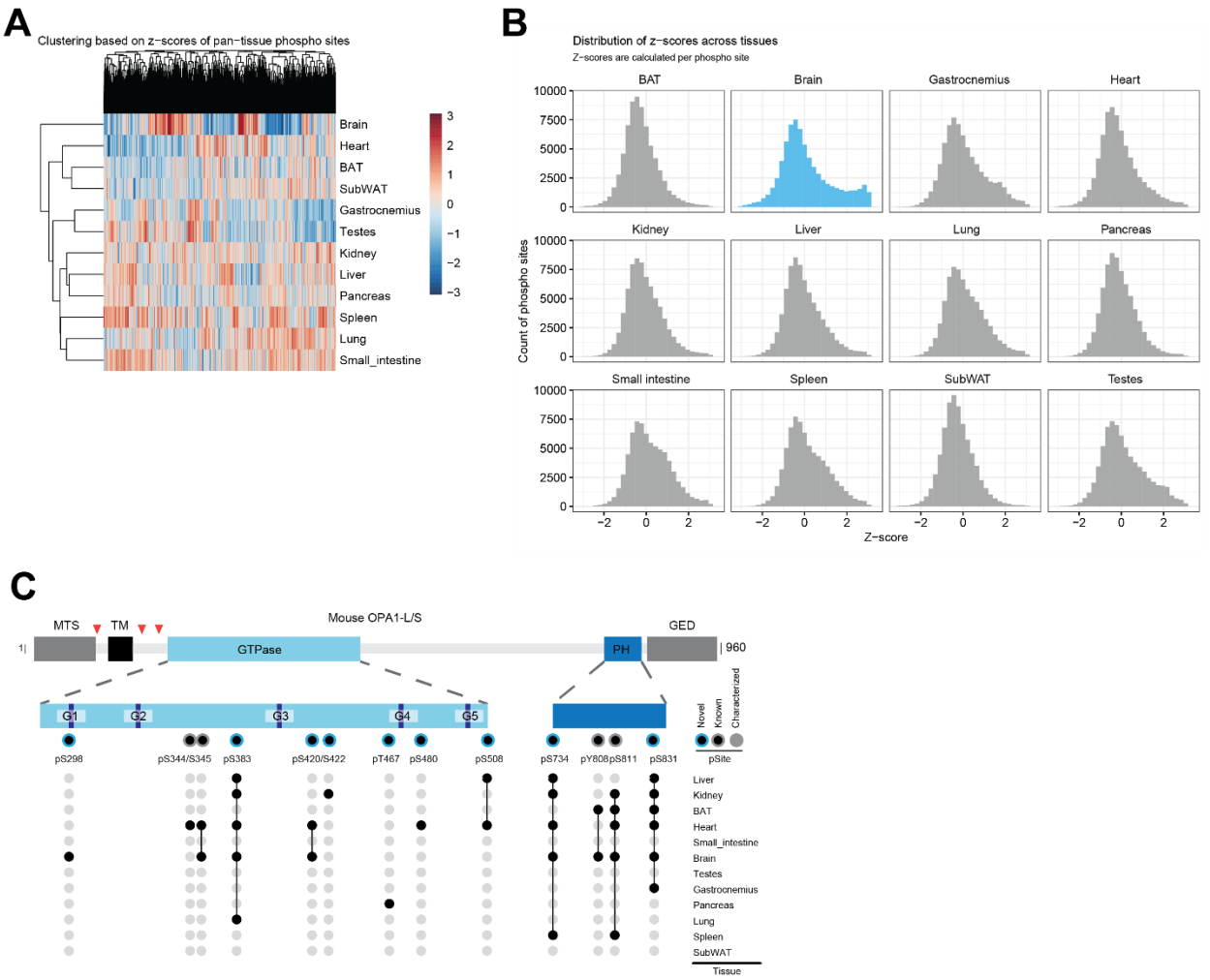

Supplementary Figure 10. Z-score based outlier analysis and phosphorylation sites on Opa1. (A) Heatmap of z-scores calculated across all tissues. Only sites that occur in all tissues were considered. (B) Distribution of phosphorylation site z-scores in each tissue, using the entire imputed dataset. (C) Protein domain representation of mouse OPA1 as shown in Figure 5D with additional phosphorylation sites not observed in brain tissue. The occurrence of OPA1 phosphorylation site within all twelve dataset is shown below. Source Data are provided as a Source Data file.

SUPPLEMENTARY NOTES

MS1 Orbitrap Scan Settings

Because Astral MS2 acquisition can be performed in parallel with the Orbitrap MS1 scan, we selected the 240,000 resolving power at 200 *m/z* scan for high-resolution MS1 scan acquisition. This scan takes just over 0.5s[5], so we selected a 0.6s cycle time (the instrument control software allows cycles times in 0.1s increments) to maximize the Orbitrap MS1 duty cycle.

MS2 Maximum Inject Time

The timing sequence for Astral analysis has been previously described by Stewart *et al*.[6] Using a maximum injection time of 3.5 ms ensures that the ion accumulation time is close to maximally parallelized with other steps in the scan sequence. This setting enables a scan rate of ~200 Hz to be maintained throughout the runs. Below, the MS1 and MS2 cycle times are plotted for our 15-minute active gradient method with a 2 Th DIA window iterating over a 380-980 m/z range (a total of 300 windows). Cycle times of ~0.6 and ~1.5s are observed for the MS1 and MS2 scans, respectively (**Supplementary Figure 1E**). Maintaining short cycle times is essential as the columns employed in this study yield median chromatographic peak widths less than 8 seconds for our 15-minute method (as shown in **Supplementary Figure 1B**).

DIA *m/z* Range

The *m/z* range iterated over during DIA analysis is a key method parameter. The size of this range limits the achievable cycle time (or the minimum isolation window width). In our experiments, we utilized a 380-980 *m/z* range, a common range used for DIA proteomics.[6–8] Enriched phosphopeptide samples could exhibit different *m/z* distributions than proteomics samples due to the mass shift from phosphorylation and increased missed cleavages[9] so we compared the use of a 380-980 *m/z* range with a 480-1080 *m/z* range for the analysis of EGF-stimulated HeLa phosphopeptides. We observe that the use of the 480-1080 *m/z* range decreases the number of phosphosites by ~6% (**Supplementary Figure 2D**), validating our use of a 380-980 *m/z* range in this study. However, we note that the optimal *m/z* range likely depends on the sample type being analyzed.

Astral AGC target

The AGC target for the Astral analyzer influences the number of charges that are targeted for each scan. We utilized a target of 5e4 (500%) for DIA phosphoproteomics. We compared this to a method using a target of 1e4 for analysis of the EGF-stimulated HeLa phosphopeptide samples. We note that there is no considerable difference in the depth achieved with these two methods (**Supplementary Figure 2E**). We note that the MS2 scan total ion current distributions are identical for both methods (**Supplementary**

Figure 2F). This observation is explained by looking at the MS2 inject time distribution, with that both methods reach the maximum injection time setting of 3.5 ms for most scans (**Supplementary Figure 2G**). The absence of an effect on phosphoproteomic depth then arises from the AGC target not being reached in either method for these particular analyses.

SUPPLEMENTARY REFERENCES

(1) Bekker-Jensen, D. B.; Bernhardt, O. M.; Hogrebe, A.; Martinez-Val, A.; Verbeke, L.; Gandhi, T.; Kelstrup, C. D.; Reiter, L.; Olsen, J. V. Rapid and Site-Specific Deep Phosphoproteome Profiling by Data-Independent Acquisition without the Need for Spectral Libraries. *Nat. Commun.* **2020**, *11* (1), 787. https://doi.org/10.1038/s41467-020-14609-1.

(2) Huttlin, E. L.; Jedrychowski, M. P.; Elias, J. E.; Goswami, T.; Rad, R.; Beausoleil, S. A.; Villén, J.; Haas, W.; Sowa, M. E.; Gygi, S. P. A Tissue-Specific Atlas of Mouse Protein Phosphorylation and Expression. *Cell* **2010**, *143* (7), 1174–1189. https://doi.org/10.1016/j.cell.2010.12.001.

(3) Giansanti, P.; Samaras, P.; Bian, Y.; Meng, C.; Coluccio, A.; Frejno, M.; Jakubowsky, H.; Dobiasch, S.; Hazarika, R. R.; Rechenberger, J.; Calzada-Wack, J.; Krumm, J.; Mueller, S.; Lee, C.-Y.; Wimberger, N.; Lautenbacher, L.; Hassan, Z.; Chang, Y.-C.; Falcomatà, C.; Bayer, F. P.; Bärthel, S.; Schmidt, T.; Rad, R.; Combs, S. E.; The, M.; Johannes, F.; Saur, D.; de Angelis, M. H.; Wilhelm, M.; Schneider, G.; Kuster, B. Mass Spectrometry-Based Draft of the Mouse Proteome. *Nat. Methods* **2022**, *19* (7), 803–811. https://doi.org/10.1038/s41592-022-01526-y.

(4) Ge, S. X.; Jung, D.; Yao, R. ShinyGO: A Graphical Gene-Set Enrichment Tool for Animals and Plants. *Bioinforma. Oxf. Engl.* **2020**, *36* (8), 2628–2629. https://doi.org/10.1093/bioinformatics/btz931.

(5) *UWPR*. https://proteomicsresource.washington.edu/instruments/orbitrapexploris480.php (accessed 2024-04-30).

(6) Stewart, H. I.; Grinfeld, D.; Giannakopulos, A.; Petzoldt, J.; Shanley, T.; Garland, M.; Denisov, E.; Peterson, A. C.; Damoc, E.; Zeller, M.; Arrey, T. N.; Pashkova, A.; Renuse, S.; Hakimi, A.; Kühn, A.; Biel, M.; Kreutzmann, A.; Hagedorn, B.; Colonius, I.; Schütz, A.; Stefes, A.; Dwivedi, A.; Mourad, D.; Hoek, M.; Reitemeier, B.; Cochems, P.; Kholomeev, A.; Ostermann, R.; Quiring, G.; Ochmann, M.; Möhring, S.; Wagner, A.; Petker, A.; Kanngiesser, S.; Wiedemeyer, M.; Balschun, W.; Hermanson, D.; Zabrouskov, V.; Makarov, A. A.; Hock, C. Parallelized Acquisition of Orbitrap and Astral Analyzers Enables High-Throughput Quantitative Analysis. *Anal. Chem.* **2023**, *95* (42), 15656–15664. https://doi.org/10.1021/acs.analchem.3c02856.

(7) Heil, L. R.; Damoc, E.; Arrey, T. N.; Pashkova, A.; Denisov, E.; Petzoldt, J.; Peterson, A. C.; Hsu, C.; Searle, B. C.; Shulman, N.; Riffle, M.; Connolly, B.; MacLean, B. X.; Remes, P. M.; Senko, M. W.; Stewart, H. I.; Hock, C.; Makarov, A. A.; Hermanson, D.; Zabrouskov, V.; Wu, C. C.; MacCoss, M. J. Evaluating the Performance of the Astral Mass Analyzer for Quantitative Proteomics Using Data-Independent Acquisition. *J. Proteome Res.* **2023**, *22* (10), 3290–3300. https://doi.org/10.1021/acs.jproteome.3c00357.

(8) Guzman, U. H.; Martinez-Val, A.; Ye, Z.; Damoc, E.; Arrey, T. N.; Pashkova, A.; Renuse, S.; Denisov, E.; Petzoldt, J.; Peterson, A. C.; Harking, F.; Østergaard, O.; Rydbirk, R.; Aznar, S.; Stewart, H.; Xuan, Y.; Hermanson, D.; Horning, S.; Hock, C.; Makarov, A.; Zabrouskov, V.; Olsen, J. V. Ultra-Fast Label-Free Quantification and Comprehensive Proteome Coverage with Narrow-Window Data-Independent Acquisition. *Nat. Biotechnol.* **2024**. https://doi.org/10.1038/s41587-023-02099-7.
(9) Molina, H.; Horn, D. M.; Tang, N.; Mathivanan, S.; Pandey, A. Global Proteomic Profiling of Phosphopeptides Using Electron Transfer Dissociation Tandem Mass Spectrometry. *Proc. Natl. Acad. Sci.* **2007**, *104* (7), 2199–2204. https://doi.org/10.1073/pnas.0611217104.